

# A characteristic based method for the calculation of three-dimensional incompressible, turbulent and steady flows in hydraulic turbomachines and installations

P. A. Govatsos<sup>\*,1</sup> and D. E. Papantonis

*Laboratory of Hydraulic Turbomachines, Department of Mechanical Engineering,  
National Technical University of Athens, Athens, Greece*

## SUMMARY

The present algorithm is developed to calculate three-dimensional incompressible, turbulent and steady flows in hydraulic turbomachines and installations. The code is based on a characteristic based method for the solution of the incompressible Navier–Stokes equations, coupling the continuity and momentum equations after the introduction of the artificial compressibility formulation. The primitive variables, pressure and velocity components are defined as functions of their values on the characteristics. The primitive variables on the characteristics are calculated by an upwind differencing scheme based on the sign of the local eigenvalue of the Jacobian matrix of the convective fluxes. The upwind scheme uses interpolation formulas of third-order accuracy. The standard  $k$ – $\varepsilon$  model is applied for the description of turbulence effects. The time discretization is obtained by the explicit Runge–Kutta method. For faster convergences to the steady state solution, a local time stepping and a mesh-sequencing scheme are used. Validation of the algorithm is performed on many two- and three-dimensional laminar and turbulent flow cases, while in the present work, the three-dimensional flow (laminar and turbulent) through a square duct with a 90° bend is presented. Finally, the code is applied for the prediction of the relative flow through the impeller of the Societe Hydrotechnique de France (SHF) water pump. The numerical results are compared with the corresponding experimental measurements. Copyright © 2000 John Wiley & Sons, Ltd.

**KEY WORDS:** artificial compressibility; hydraulic turbomachines; incompressible flows; Navier–Stokes equations; Riemann solver; SHF water pump

## 1. INTRODUCTION

During the last decade the capabilities of computational fluid dynamics (CFD) have increased significantly and advanced methods have penetrated from aerodynamics and aircraft design into hydrodynamic installations and hydromachine design [1,2]. The most common CFD

---

\* Correspondence to: Elliniki Technodomiki A.E., 78a Louizis Riankoun Str., GR-115 23 Athens, Greece.

<sup>1</sup> E-mail: govats@fluid.mech.ntua.gr

methods used in the field of hydraulic turbomachines and installations can be classified as follows.

The classical two-dimensional potential flow codes [3,4], which were useful for approximately two-dimensional cascades, like the mid-span section of stay vanes, axial runners and guide vane cascades. For radial and mixed flow machines, two different ways of study were attempted very early on with the arrival of numerical algorithms, such as finite differences or finite elements. On one hand, you had the two-dimensional and quasi-three-dimensional Euler methods [5], which had the advantage of taking into account the rotational effects but without calculating the three-dimensional effects. On the other hand, there was the three-dimensional potential flow methods [6], which cover the three-dimensional effects but only as long as they are irrotational. As the flow in a typical Francis runner is a rotational one, a three-dimensional potential flow analysis needs a superposition technique to satisfy the Kutta condition and is not valid for strong swirl downstream of the runner. Although both methods just tell parts of the story, they became popular because only Poisson equation solvers were necessary.

The three-dimensional Euler methods [7–9] represent a significant progress in comparison with the above-mentioned methods. The rotational and three-dimensional effects are calculated by solving the momentum equations with velocity and pressure as primitive variables, but the calculation of the viscous effects is impossible. So all losses, except of the viscous losses, can be calculated and all inviscid secondary flows, inviscid vortices and momentum driven reverse flow regions can be modelled by a three-dimensional Euler method.

By applying one of the Navier–Stokes codes in addition to the use of the turbulence model, it is possible to calculate viscous losses. Although the ratio between the obtained accuracy and the necessary investment is still rather unfavourable, many Navier–Stokes methods are applied in the field of hydraulic turbomachines.

The development of solution methodologies [10–12] for the Navier–Stokes equations has received considerable attention recently. The solution of incompressible flows in primitive variables involves the need of coupling the changes in the velocity field with the changes in the pressure field while at the same time the continuity should be satisfied. For three-dimensional incompressible flows, most of the methods using primitive variables can be classified into two broad categories.

The first category is the pressure Poisson method, as first introduced by Harlow and Welch [13]. In this method, at each iteration a Poisson ‘correction’ equation [14], which is formed from the momentum equations, is solved for the pressure to satisfy the continuity equation at the next iteration [13,14].

The other category is that of artificial compressibility and was first introduced by Chorin [15] for steady flow cases. In the artificial compressibility (or pseudo-compressibility) formulation, a time derivative of the pressure is added to the continuity equation; therefore, a coupling of the primitive variables (pressure and velocity) is obtained. Over the last years many authors have used similar methods in computing steady and unsteady incompressible flows [16–18].

The artificial compressibility formulation transforms the incompressible Euler equations into a totally hyperbolic system; therefore, numerical methods that have initially been developed for the compressible Euler and Navier–Stokes can also be extended to incompressible flows. In this method a pressure term instead of a time derivative of pressure is added to the continuity equation. A combination of the penalty and pseudo-compressibility method for solving Navier–Stokes equations has also been proposed by other authors [19].

The present code uses a characteristic based method, which exploits the hyperbolic properties of the incompressible inviscid equations as they are introduced by the pseudo-compressibility formulation. In the past, Eberle [20] developed a characteristic flux averaging scheme for an ideal gas, and the method has been reformulated for real gas problems by other authors [21,22]. The present method defines the primitive variables (pressure and velocity components) as functions of their corresponding values on the characteristics. Consequently, the values on the characteristics are calculated by an upwind differencing scheme based on the sign of the local eigenvalue of the Jacobian matrix of the convective fluxes. The Navier–Stokes terms are discretized by an upwind-type scheme [24].

The turbulence effects are described by the  $k$ – $\varepsilon$  model of Launder and Spalding [23], together with the standard wall functions for the boundary conditions. The discretization of turbulence equations is obtained by an upwind-type scheme of second-order accuracy.

The time integration is obtained by a multistage (fourth-order) Runge–Kutta scheme [24,25], and, for faster convergence to the steady state solution, a mesh-sequencing scheme is used.

## 2. GOVERNING EQUATIONS AND NUMERICAL METHOD

In the present method, the governing equations are divided into two groups. The first group includes the fluid motion (Navier–Stokes) equations and the second group includes the equations for the turbulence modelling ( $k$ – $\varepsilon$  equations).

### 2.1. Fluid flow equations, artificial compressibility and characteristic flux extrapolation method

The non-dimensional, incompressible Navier–Stokes equations, by using the artificial compressibility formulation and general curvilinear co-ordinates  $\xi = \xi(x, y, z)$ ,  $\eta = \eta(x, y, z)$  and  $\zeta = \zeta(x, y, z)$ , can be written as

$$(JU)_t + E_\xi + F_\eta + G_\zeta = \frac{1}{Re} \cdot (R_\xi + S_\eta + T_\zeta) + a \cdot P \quad (1)$$

where  $Re$  is the Reynolds number and  $U$  is the unknown solution vector

$$U = (p/\beta, u, v, w)^T$$

The pressure  $p$  and velocity Cartesian components  $u$ ,  $v$  and  $w$  (in the  $x$ -,  $y$ - and  $z$ -directions respectively) are used as primitive variables. The artificial compressibility is denoted  $\beta$ , and its value is chosen to ensure the fastest convergence to the steady state. By systematic numerical experimentations, it has been found that the best convergence rate is obtained with  $\beta = 1$ . The vector  $P$  includes the terms due to the relative rotating system of the impeller and namely the Coriolis and centrifugal acceleration terms

$$P = (0, 0, \Omega^2 y + 2\Omega w, \Omega^2 z - 2\Omega v)^T$$

where  $\Omega$  is the speed of rotation of the relative system around the  $x$ -axis. The parameter  $a$  of Equation (1) is used to define the type of flow equation. For  $a = 1$ , the system of equations is referred to as rotating flow cases, and  $u$ ,  $v$  and  $w$  are the components of the relative velocity. For fixed (no rotating) flow cases, the vector  $P$  is neglected,  $a = 0$  and  $u$ ,  $v$  and  $w$  are the components of the absolute velocity.

The inviscid flux vectors  $E$ ,  $F$  and  $G$  and the viscous ones  $R$ ,  $S$  and  $T$  can be written by the superposition of the respective Cartesian inviscid ( $E'$ ,  $F'$ ,  $G'$ ) and viscous ( $R'$ ,  $S'$ ,  $T'$ ) fluxes as

$$\begin{aligned} E &= J(E' \cdot \zeta_x + F' \cdot \zeta_y + G' \cdot \zeta_z) & R &= J(R' \cdot \zeta_x + S' \cdot \zeta_y + T' \cdot \zeta_z) \\ F &= J(E' \cdot \eta_x + F' \cdot \eta_y + G' \cdot \eta_z) & S &= J(R' \cdot \eta_x + S' \cdot \eta_y + T' \cdot \eta_z) \\ G &= J(E' \cdot \zeta_x + F' \cdot \zeta_y + G' \cdot \zeta_z) & T &= J(R' \cdot \zeta_x + S' \cdot \zeta_y + T' \cdot \zeta_z) \end{aligned}$$

where the Cartesian fluxes are defined as

$$\begin{aligned} E' &= (u, u^2 + p, u \cdot v, u \cdot w) & R' &= (0, \tau_{xx}, \tau_{xy}, \tau_{xz}) \\ F' &= (v, u \cdot v, v^2 + p, v \cdot w) & S' &= (0, \tau_{xy}, \tau_{yy}, \tau_{yz}) \\ G' &= (w, u \cdot w, v \cdot w, w^2 + p) & T' &= (0, \tau_{xz}, \tau_{yz}, \tau_{zz}) \end{aligned}$$

The terms  $\tau_{ij}$  ( $i, j = x, y, z$ ) are the viscous stresses, while  $J$  is the Jacobian of the transformation  $\zeta = \zeta(x, y, z)$ ,  $\eta = \eta(x, y, z)$  and  $\zeta = \zeta(x, y, z)$ , from Cartesian to generalized co-ordinates

$$J = x_\zeta \cdot (y_\eta \cdot z_\zeta - y_\zeta \cdot z_\eta) - x_\eta \cdot (y_\zeta \cdot z_\zeta - y_\zeta \cdot z_\zeta) + x_\zeta \cdot (y_\zeta \cdot z_\eta - y_\eta \cdot z_\zeta)$$

Except the terms of the viscous stresses, the indices  $x$ ,  $y$  and  $z$  denote partial derivatives. The viscous stresses can be written as

$$\begin{aligned} \tau_{xx} &= \frac{2}{3} \cdot \bar{\mu} \cdot (2 \cdot u_x - v_y - w_z) & \tau_{yy} &= \frac{2}{3} \cdot \bar{\mu} \cdot (2 \cdot v_y - u_x - w_z) & \tau_{zz} &= \frac{2}{3} \cdot \bar{\mu} \cdot (2 \cdot w_z - v_y - u_x) \\ \tau_{xy} &= \bar{\mu} \cdot (u_y - v_x) & \tau_{xz} &= \bar{\mu} \cdot (u_z - w_x) & \tau_{yz} &= \bar{\mu} \cdot (w_y - v_z) \end{aligned}$$

where  $\bar{\mu}$  is the effective viscosity defined as

$$\bar{\mu} = \mu + \mu_t$$

with  $\mu$  being the laminar viscosity of the fluid and  $\mu_t$  being the turbulent viscosity calculated according to the  $k$ - $\varepsilon$  model of turbulence [23].

Neglecting the viscous flux vectors  $R$ ,  $S$ ,  $T$  and the vector  $P$  of the rotating terms from the Navier–Stokes equations (1), the incompressible Euler equations are obtained

$$(JU)_t + E_\xi + F_\eta + G_\zeta = 0 \tag{2}$$

In the present work, a characteristic based method (a local Riemann solver) is presented which exploits the hyperbolic properties of the above system of equations. The method is used for the discretization of the convective part of the Navier–Stokes equations and is initially used for the calculation of two-dimensional steady laminar flows [18].

The Euler equations can be discretized using a finite volume scheme. All quantities (pressure and velocity components) are considered to be located at the centre of the corresponding volume. In three dimensions this can be done by considering a volume  $(i, j, k)$  (Figure 1) with cell faces  $(i + \frac{1}{2}, j, k)$ ,  $(i - \frac{1}{2}, j, k)$  in the  $x$ -direction;  $(i, j + \frac{1}{2}, k)$ ,  $(i, j - \frac{1}{2}, k)$  in the  $y$ -direction; and  $(i, j, k + \frac{1}{2})$ ,  $(i, j, k - \frac{1}{2})$  in the  $z$ -direction respectively.

Using the finite volume concept, the Euler equations are written as

$$(JU)_t + E_{i+1/2,j,k} - E_{i-1/2,j,k} + F_{i,j+1/2,k} - F_{i,j-1/2,k} + G_{i,j,k+1/2} - G_{i,j,k-1/2} = 0 \tag{3}$$

A simpler form than that of Equation (3) can be chosen to analyse the incompressible Euler equations. This can be done by splitting the system of equations into three one-dimensional equations

$$1/3 \cdot (JU)_t + E_\xi = 0 \tag{4a}$$

$$1/3 \cdot (JU)_t + F_\eta = 0 \tag{4b}$$

$$1/3 \cdot (JU)_t + G_\zeta = 0 \tag{4c}$$

In the following paragraphs, the analysis of the method for Equation (4a) is presented. This equation can be used for the development of the local Riemann solution in the  $x$ -direction.

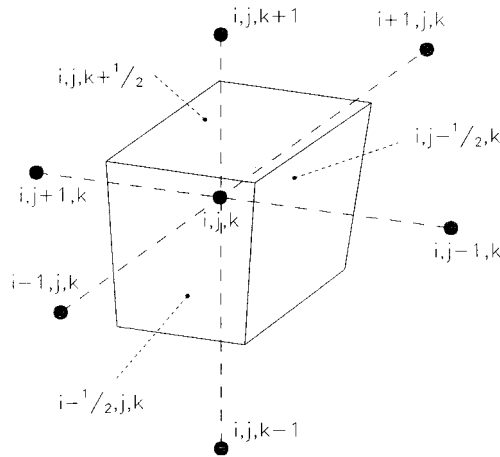


Figure 1. A finite volume  $(i, j, k)$  with its volume faces.

Similarly, Equations (4b) and (4c) can be analysed, resulting in a local Riemann solution in the  $y$ - and  $z$ -directions respectively. The term  $1/3$  of the time derivative will be included in the calculation of the local time step so it is neglected in the following equations. The non-conservative form of Equation (4a) is

$$\frac{1}{\beta} p_t + u_\xi \zeta_x + v_\xi \zeta_y + w_\xi \zeta_z = 0 \quad (5a)$$

$$u_t + u_\xi (u \zeta_x + v \zeta_y + w \zeta_z) + u (u_\xi \zeta_x + v_\xi \zeta_y + w_\xi \zeta_z) + \zeta_x p_\xi = 0 \quad (5b)$$

$$v_t + v_\xi (u \zeta_x + v \zeta_y + w \zeta_z) + v (u_\xi \zeta_x + v_\xi \zeta_y + w_\xi \zeta_z) + \zeta_y p_\xi = 0 \quad (5c)$$

$$w_t + w_\xi (u \zeta_x + v \zeta_y + w \zeta_z) + w (u_\xi \zeta_x + v_\xi \zeta_y + w_\xi \zeta_z) + \zeta_z p_\xi = 0 \quad (5d)$$

In the previous system of equations, the space derivatives are usually calculated by the initial data at the time level  $n$ . In order to perform time integration of Equations (4a)–(4c), the updated values of the vector  $U = (p/\beta, u, v, w)^T$  at the time level  $(n+1)$  can be defined by a linear Taylor series expansion around the known previous time level (Figure 2). The vector  $U$  can be defined as function of the  $U_j$  values, which are inside the limits of a stable integration [26]

$$U = U_j + \Delta \xi U_\xi + U_t \Delta t, \quad U_t = \frac{U - U_j}{\Delta t} - U_\xi \frac{\Delta \xi}{\Delta t} \quad (6)$$

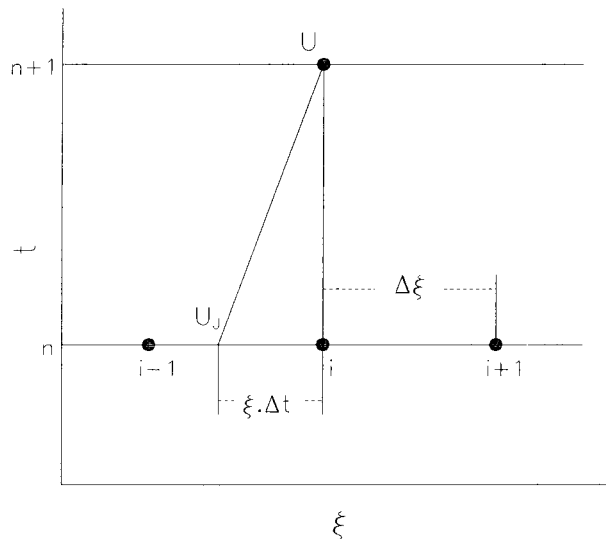


Figure 2. Schematic presentation of the characteristic method.

where the interval  $\Delta\xi = \xi' \cdot \Delta t$  is defined by introducing a wave speed  $\xi'$ . The line with the slope  $1/\xi'$  is the characteristic.

It is clear that the term  $\xi'$  is not a real physical speed, as  $\xi$  is dimensionless, and therefore  $\xi'$  is an inverse time. Following a dimensional analysis, in order to enter a physical wave speed with a proper dimension, a wave speed  $\lambda$  is introduced via

$$\xi' = \lambda \sqrt{\xi_x^2 + \xi_y^2 + \xi_z^2}$$

After the introduction of the wave speed  $\lambda$ , Equation (6) yields

$$U_t = \frac{U - U_j}{\Delta t} - U_\xi \lambda \sqrt{\xi_x^2 + \xi_y^2 + \xi_z^2} \quad (7)$$

By substitution of Equation (7) into Equations (5a)–(5d), the following equations are obtained:

$$\frac{1}{\beta} \frac{1}{\Delta t \sqrt{\xi_x^2 + \xi_y^2 + \xi_z^2}} (p - p_j) - \frac{1}{\beta} p_\xi \lambda + u_\xi \bar{x} + v_\xi \bar{y} + w_\xi \bar{z} = 0 \quad (8a)$$

$$\frac{1}{\Delta t \sqrt{\xi_x^2 + \xi_y^2 + \xi_z^2}} (u - u_j) + u_\xi (\lambda - \lambda_0) + u(u_\xi \bar{x} + v_\xi \bar{y} + w_\xi \bar{z}) + p_\xi \bar{x} = 0 \quad (8b)$$

$$\frac{1}{\Delta t \sqrt{\xi_x^2 + \xi_y^2 + \xi_z^2}} (v - v_j) + v_\xi (\lambda - \lambda_0) + v(u_\xi \bar{x} + v_\xi \bar{y} + w_\xi \bar{z}) + p_\xi \bar{y} = 0 \quad (8c)$$

$$\frac{1}{\Delta t \sqrt{\xi_x^2 + \xi_y^2 + \xi_z^2}} (w - w_j) + w_\xi (\lambda - \lambda_0) + w(u_\xi \bar{x} + v_\xi \bar{y} + w_\xi \bar{z}) + p_\xi \bar{z} = 0 \quad (8d)$$

where

$$\lambda_0 = u \cdot \bar{x} + v \cdot \bar{y} + w \cdot \bar{z} \quad \text{and} \quad \bar{a} = \frac{\xi_a}{\sqrt{\xi_x^2 + \xi_y^2 + \xi_z^2}}, \quad a = x, y, z$$

The spatial derivatives of  $u_x$ ,  $w_x$  and  $p_x$  can be calculated from the above three equations. The method of Riemann [26] is used for the calculation of the above equations and a similar consideration has also been done by Eberle [25] for the compressible Euler equations. According to this consideration, at each time step the system of equations is zero so it can be multiplied by an arbitrary coefficient. After the summation of the three equations, the resulting equation will also be equal to zero

$$\begin{aligned} & \frac{1}{\Delta t \sqrt{\xi_x^2 + \xi_x^2 + \xi_x^2}} \left[ \frac{1}{\beta} a(p - p_j) + b(u - u_j) + c(v - v_j) + d(w - w_j) \right] \\ & + p_\xi \left[ -a \frac{\lambda}{\beta} + b\bar{x} + c\bar{y} + d\bar{z} \right] + u_\xi [a\bar{x} + b(\lambda_0 - \lambda + u\bar{x}) + cv\bar{x} + dw\bar{x}] \\ & + v_\xi [a\bar{y} + c(\lambda_0 - \lambda + v\bar{y}) + bu\bar{y} + dw\bar{y}] + w_\xi [a\bar{z} + d(\lambda_0 - \lambda + w\bar{z}) + bu\bar{z} + cv\bar{z}] = 0 \end{aligned} \quad (9)$$

where  $a$ ,  $b$ ,  $c$  and  $d$  are the coefficients for the multiplication of Equations (8a)–(8d) respectively. After the definition of the coefficients of the partial space derivatives are set to zero, the following equation system is obtained:

$$\frac{1}{\beta} a(p - p_j) + b(u - u_j) + c(v - v_j) + d(w - w_j) = 0 \quad (10a)$$

$$-a \frac{\lambda}{\beta} + b\bar{x} + c\bar{y} + d\bar{z} = 0 \quad (10b)$$

$$a\bar{x} + b(\lambda_0 - \lambda + u\bar{x}) + cv\bar{x} + dw\bar{x} = 0 \quad (10c)$$

$$a\bar{y} + c(\lambda_0 - \lambda + v\bar{y}) + bu\bar{y} + dw\bar{y} = 0 \quad (10d)$$

$$a\bar{z} + d(\lambda_0 - \lambda + w\bar{z}) + bu\bar{z} + cv\bar{z} = 0 \quad (10e)$$

The coefficients  $a$ ,  $b$ ,  $c$  and  $d$  can be determined by solving the system of Equations (10b)–(10e). A non-trivial solution is obtained for each of the eigenvalues of the above system

$$\lambda_0 = u \cdot \bar{x} + v \cdot \bar{y} + w \cdot \bar{z} \quad (11a)$$

$$\lambda_1 = \lambda_0 + \sqrt{\lambda_0^2 + \beta} \quad (11b)$$

$$\lambda_2 = \lambda_0 - \sqrt{\lambda_0^2 + \beta} \quad (11c)$$

For the eigenvalue  $\lambda = \lambda_0$ , Equations (11a)–(11c) give

$$a = \frac{b\bar{x} + c\bar{y} + d\bar{z}}{\lambda_0} \beta$$

By substitution of the last equation into Equation (10a), the following equation arises:

$$b \{ \bar{x}(p - p_0) + (u - u_0)\lambda_0 \} + c \{ \bar{y}(p - p_0) + (v - v_0)\lambda_0 \} + d \{ \bar{z}(p - p_0) + (w - w_0)\lambda_0 \} = 0 \quad (12)$$

The subscript '0' denotes that the Equation (12) corresponds to the zeroth eigenvalue  $\lambda = \lambda_0$ . The last equation is satisfied regardless of the values of the coefficients  $b$ ,  $c$  and  $d$ . Therefore, the terms into the brackets must be zero, and thus the following equations are obtained:

$$\bar{x}(w - w_0) - \bar{z}(u - u_0) = 0 \quad (13a)$$

$$\bar{x}(v - v_0) - \bar{y}(u - u_0) = 0 \quad (13b)$$

Similarly with the above equations, for the zeroth eigenvalue  $\lambda_0$ , the following equations are obtained for the eigenvalues  $\lambda_1$  and  $\lambda_2$ :

$$(p - p_1) + \lambda_1[\bar{x}(u - u_1) + \bar{y}(v - v_1) + \bar{z}(w - w_1)] = 0 \quad (14a)$$

$$(p - p_2) + \lambda_2[\bar{x}(u - u_2) + \bar{y}(v - v_2) + \bar{z}(w - w_2)] = 0 \quad (14b)$$

The values  $p_j$ ,  $u_j$ ,  $v_j$  and  $w_j$ , with  $j = 0, 1, 2$ , are the values of the pressure and velocity components (primitive variables) on the three characteristics and Equations (13) and (14) are the characteristic equations or Riemann invariants. From the solution of the previous equations, the primitive variables  $p$ ,  $u$ ,  $v$  and  $w$  are given as functions of their characteristic values

$$u = \bar{x} \cdot R_1 + \bar{z} \cdot (\bar{z} \cdot u_0 - \bar{x} \cdot w_0) + \bar{y} \cdot (\bar{y} \cdot u_0 - \bar{x} \cdot v_0) \quad (15a)$$

$$v = \bar{y} \cdot R_1 + \bar{x} \cdot (\bar{x} \cdot v_0 - \bar{y} \cdot u_0) + \bar{z} \cdot (\bar{z} \cdot v_0 - \bar{y} \cdot w_0) \quad (15b)$$

$$w = \bar{z} \cdot R_1 + \bar{x} \cdot (\bar{x} \cdot w_0 - \bar{z} \cdot u_0) + \bar{y} \cdot (\bar{y} \cdot w_0 - \bar{z} \cdot v_0) \quad (15c)$$

$$p = \frac{\lambda_1 \cdot k_2 - \lambda_2 \cdot k_1}{\sqrt{\lambda_0^2 + \beta}} \quad (15d)$$

where the coefficients  $k_1$ ,  $k_2$  and  $R_1$  are defined as

$$k_1 = p_1 + \lambda_1 \cdot (\bar{x} \cdot u_1 + \bar{y} \cdot v_1 + \bar{z} \cdot w_1)$$

$$k_2 = p_2 + \lambda_2 \cdot (\bar{x} \cdot u_2 + \bar{y} \cdot v_2 + \bar{z} \cdot w_2)$$

$$R_1 = \frac{0.5}{\sqrt{\lambda_0^2 + \beta}} [(p_1 - p_2) + (\lambda_1 u_1 - \lambda_2 u_2) \bar{x} + (\lambda_1 v_1 - \lambda_2 v_2) \bar{y} + (\lambda_1 w_1 - \lambda_2 w_2) \bar{z}]$$

The values of the pressure and velocity components obtained from Equations (15a)–(15d) are used for the calculation of the inviscid flux,  $E$ , on the cell face of the computational volume.

The characteristics values  $p_j$ ,  $u_j$  and  $w_j$ , with  $j = 0, 1, 2$ , are defined by upwind differencing from the left or the right side of the cell face according to sign of the eigenvalues

$$U_{i+1/2}^j = \begin{pmatrix} p_j \\ u_j \\ v_j \\ w_j \end{pmatrix}_{i+1/2} = \frac{1}{2} \cdot [(1 + \text{sign } \lambda_j) \cdot U^- + (1 - \text{sign } \lambda_j) \cdot U^+]$$

where  $U_{i+1/2}^j$  is a vector containing the characteristic values for each  $j = 0, 1, 2$  and  $U^-$ ,  $U^+$  are the vectors of the characteristics variables from the left and the right side of the control volume respectively. A third-order interpolation formula [21] is employed to increase the accuracy of the scheme

$$(U_{i+1/2})^- = \frac{5 \cdot U_i - U_{i-1} + 2 \cdot U_{i+1}}{6}, \quad (U_{i+1/2})^+ = \frac{5 \cdot U_{i+1} - U_{i+2} + 2 \cdot U_i}{6}$$

These interpolation formulas have also been used in the past [19] for the solution of the compressible Euler and Navier–Stokes equations providing satisfactory accuracy and convergence properties.

In this section, the analysis concerns the inviscid flux  $E$ . Similar analysis is used for the solution of vectors  $F$  and  $G$  in the  $y$ - and  $z$ -directions respectively.

The solution of the Navier–Stokes equations requires also the discretization of the viscous terms. For this purpose, an ‘upwind’ type scheme for the cross-derivatives of the viscous fluxes and central discretization for the second-order derivatives was adopted [22]. Similar schemes have been used successfully in the past for subsonic and supersonic flows.

## 2.2. Turbulence equations $k$ – $\varepsilon$ and the law of the wall

For the modelization of turbulence effects, the standard  $k$ – $\varepsilon$  turbulence model [23] is applied. Close to the solid walls viscous effects become considerable and such a model does not lead to acceptable predictions. In the current numerical procedure, the wall functions [23,28] method is applied for the volumes adjacent to solid walls.

The turbulent viscosity  $\mu_t$  is calculated according to the  $k$ – $\varepsilon$  turbulence model

$$\mu_t = Re \cdot C_d \cdot \frac{k^2}{\varepsilon}$$

where  $k$  is the turbulence kinetic energy,  $\varepsilon$  is the dissipation rate of the turbulence kinetic energy and  $C_d$  is a scalar constant for isotropic turbulence. The  $k$ – $\varepsilon$  turbulence model of Launder and Spalding [17] is chosen because of its capability to describe accurately and efficiently a variety of flows [23,25]. The momentum equations for  $k$  and  $\varepsilon$  can be written

$$(JU_{ke})_t + E_{ke\varepsilon\zeta} + F_{ke\eta} + G_{ke\zeta} = \frac{1}{Re} \cdot (R_{ke\varepsilon\zeta} + S_{ke\eta} + T_{ke\varepsilon\zeta} + P_{ke})$$

where

$$U_{k\varepsilon} = \begin{pmatrix} k \\ \varepsilon \end{pmatrix}$$

$$P_{k\varepsilon} = J \cdot \begin{pmatrix} \Theta - Re \cdot \varepsilon \\ (t_1 \cdot \Theta - Re \cdot t_2 \cdot \varepsilon) \cdot \varepsilon / k \end{pmatrix}$$

$$E_{k\varepsilon} = J \cdot \begin{pmatrix} (u \cdot \zeta_x + v \cdot \zeta_y + w \cdot \zeta_z) \cdot k \\ (u \cdot \zeta_x + v \cdot \zeta_y + w \cdot \zeta_z) \cdot \varepsilon \end{pmatrix}$$

$$R_{k\varepsilon} = J \cdot \begin{pmatrix} \mu_t \cdot (d_1 \cdot k_\xi + d_4 \cdot k_\eta + d_5 \cdot k_\zeta) / \sigma_k \\ \mu_t \cdot (d_1 \cdot \varepsilon_\xi + d_4 \cdot \varepsilon_\eta + d_5 \cdot \varepsilon_\zeta) / \sigma_\varepsilon \end{pmatrix}$$

$$F_{k\varepsilon} = J \cdot \begin{pmatrix} (u \cdot \eta_x + v \cdot \eta_y + w \cdot \eta_z) \cdot k \\ (u \cdot \eta_x + v \cdot \eta_y + w \cdot \eta_z) \cdot \varepsilon \end{pmatrix}$$

$$S_{k\varepsilon} = J \cdot \begin{pmatrix} \mu_t \cdot (d_4 \cdot k_\xi + d_2 \cdot k_\eta + d_6 \cdot k_\zeta) / \sigma_k \\ \mu_t \cdot (d_4 \cdot \varepsilon_\xi + d_2 \cdot \varepsilon_\eta + d_6 \cdot \varepsilon_\zeta) / \sigma_\varepsilon \end{pmatrix}$$

$$G_{k\varepsilon} = J \cdot \begin{pmatrix} (u \cdot \zeta_x + v \cdot \zeta_y + w \cdot \zeta_z) \cdot k \\ (u \cdot \zeta_x + v \cdot \zeta_y + w \cdot \zeta_z) \cdot \varepsilon \end{pmatrix}$$

$$T_{k\varepsilon} = J \cdot \begin{pmatrix} \mu_t \cdot (d_5 \cdot k_\xi + d_6 \cdot k_\eta + d_3 \cdot k_\zeta) / \sigma_k \\ \mu_t \cdot (d_5 \cdot \varepsilon_\xi + d_6 \cdot \varepsilon_\eta + d_3 \cdot \varepsilon_\zeta) / \sigma_\varepsilon \end{pmatrix}$$

and the coefficients  $d_1, d_2, d_3, d_4, d_5$  and  $d_6$  are defined as

$$d_1 = \zeta_x^2 + \zeta_y^2 + \zeta_z^2, \quad d_2 = \eta_x^2 + \eta_y^2 + \eta_z^2, \quad d_3 = \zeta_x^2 + \zeta_y^2 + \zeta_z^2,$$

$$d_4 = \zeta_x \eta_x + \zeta_y \eta_y + \zeta_z \eta_z, \quad d_5 = \zeta_x \zeta_x + \zeta_y \zeta_y + \zeta_z \zeta_z, \quad d_6 = \zeta_x \eta_x + \zeta_y \eta_y + \zeta_z \eta_z$$

The production rate of the turbulent kinetic energy is defined as

$$\Theta = 2 \cdot \mu_t \cdot (u_x^2 + v_y^2 + w_z^2) + \mu_t \cdot [(u_y + v_x)^2 + (u_z + w_x)^2 + (v_z + w_y)^2]$$

The turbulence model has five constants. The following values are commonly used:

$$C_d = 0.09, \quad t_1 = 1.44, \quad t_2 = 1.92, \quad \sigma_k = 0.9, \quad \sigma_\varepsilon = 1.22$$

In the present work, the turbulence equations  $k$ - $\varepsilon$  are numerically decoupled from the Navier–Stokes equations. Specifically, at each iteration the  $k$ - $\varepsilon$  equations are updated using the mean flow quantities just computed. The fluxes  $E_{k\varepsilon}$ ,  $F_{k\varepsilon}$  and  $G_{k\varepsilon}$  are discretized by a second upwind differencing method [24]. The variables  $k$  and  $\varepsilon$  are defined from Equation (2), on the left or the right side of the cell face according to the sign of the eigenvalue  $\lambda_0$ . A similar scheme is adopted for the discretization of the viscous fluxes  $R$ ,  $S$  and  $T$  of the fluxes  $R_{k\varepsilon}$ ,  $S_{k\varepsilon}$  and  $T_{k\varepsilon}$ .

The application of several modified turbulence models [27], in order to take into account the rotational effects, has not given numerical results essentially different than those obtained from the standard  $k$ - $\varepsilon$  turbulence model.

The above  $k$ - $\varepsilon$  model is only valid in regions with homogeneous turbulence. Near the solid walls, viscous effects become dominant and such a model does not lead to acceptable predictions. For the present calculations it is used for treating the adjacent wall regions. According to the procedure of wall functions, the region close to the solid wall is divided into two sub-layers. A laminar sub-layer, where purely viscous effects are dominant, and a turbulent sub-layer. The profile of the velocity  $U_P$  parallel to the wall at the first grid node  $P$  from the wall is

$$|U_P| = u^\# y_P^\dagger \quad \text{for laminar sub-layer } y_P^\dagger < 11.63$$

$$|U_P| = \frac{u^\#}{\kappa} \ln(E y_P^\dagger) \quad \text{for turbulent sub-layer } y_P^\dagger > 11.63$$

where  $y_P^\dagger = Re(\rho y_P u^\# / \mu)$  is the dimensionless distance of node  $P$  from the wall and  $u^\# = \sqrt{\tau_w / Re \rho}$  is the friction velocity. The other variables are defined as  $\tau_w$  is the wall shear stress,  $y_P$  is the normal distance of the node  $P$  from the wall,  $E = 9.79$  is a roughness parameter and  $\kappa = 0.419$  is the Von Karman constant. From the previous equations, the shear stress  $\tau_w$  is calculated and assuming that the shear stress is constant near the wall, the kinetic energy and the dissipation rate of the turbulence energy at the node are equal to

$$k_P = \frac{u^\#}{\sqrt{c_d}}, \quad \varepsilon_P = \frac{u^\#{}^3}{\kappa y_P}$$

### 2.3. Boundary conditions

For the numerical solution of the governing differential equations, boundary conditions must be defined on the boundaries of the computational domain. Generally, the following types of boundaries can be treated: inlet, outlet, symmetry plane and solid walls.

**2.3.1. Inlet.** On the inlet boundary the velocity profiles are specified and the pressure second derivative is set equal to zero. The kinetic energy and the dissipation of turbulence energy are estimated by the following empirical relations:

$$k = 0.03 \cdot \bar{u}^2, \quad \varepsilon = \frac{C_d \cdot k^{1.5}}{0.005 \cdot D_{in}}$$

where  $D_{in}$  is the reference inlet diameter and  $\bar{u}$  is the average inlet velocity.

2.3.2. *Outlet.* It is supposed that the flow is extended over a sufficiently long domain so that it can be considered as fully developed at the exit section. Thus, for any variable, the second derivative is set equal to zero, with an exception made for the pressure, which is taken equal to its reference value.

2.3.3. *Symmetry axis.* The first derivatives of all variables are set equal to zero, except for the vertical component of the velocity, which is instead set equal to zero.

2.3.4. *Solid walls.* On the solid surfaces, the velocity components and the pressure normal derivative are set equal to zero. For the turbulent variables,  $k$  and  $\varepsilon$ , the standard wall functions are applied.

#### 2.4. Time integration of the incompressible and turbulence equations

For the time integration of the Navier–Stokes and  $k$ – $\varepsilon$  equations, an explicit fourth-order Runge–Kutta time stepping method was employed. The Runge–Kutta time stepping method [24,25] can be written as

$$U^1 = U^n + 0.25 \cdot \Delta t \cdot \bar{Z}(U^n)$$

$$U^2 = U^n + 0.33 \cdot \Delta t \cdot \bar{Z}(U^1)$$

$$U^3 = U^n + 0.50 \cdot \Delta t \cdot \bar{Z}(U^2)$$

$$U^{n+1} = U^n + 1.0 \cdot \Delta t \cdot \bar{Z}(U^3)$$

where

$$\bar{Z}(U) = -E_\xi - F_\eta - G_\zeta + R_\xi + S_\eta + T_\zeta + P$$

For faster convergence to the steady state solution, a local time stepping technique is used

$$\Delta t = \frac{\text{CFL}}{\max(|\lambda_0|, |\lambda_1|, |\lambda_2|)_{i,j,k}}$$

where CFL is the Courant–Friedrich–Lewy number. The values of CFL for the current calculations are taken to be between 0.8 and 1.2.

#### 2.5. Solution of the discretized equations

The steps of the solution procedure can be outlined as follows:

- (a) Guess all the necessary initial variables.
- (b) Compute on the solid walls the slip parallel velocity and boundary variables  $k$ – $\varepsilon$  (wall functions).

- (c) Solve the incompressible equations.
- (d) Solve the turbulence equations using the mean flow quantities just computed.
- (e) Update the turbulence viscosity.
- (f) Update the variables, return to step (b) and repeat the process until convergence.

It should be mentioned that a mesh-sequencing scheme [29] is used to reduce the computing time. The computer time for the convergence to the steady state solution is dependent on the initial estimation of the primitive variables. The algorithm solves the flow problem using two coarse grids and succeeds in a better initial estimation for the final calculation at the formal fine grid. Each coarse grid is constructed by neglecting every second node of the next finer grid, in each direction (Figure 3; eight volumes 1–8 of the fine grid are merged into one volume of the coarse grid). Particularly, for a  $IE \times JE \times KE$  grid, the two coarse grids are the following:

$$\frac{IE + 3}{4} \times \overset{2^{nd} \text{ stage}}{\frac{JE + 3}{4}} \times \frac{KE + 3}{4} \Rightarrow \frac{IE + 1}{2} \times \overset{1^{st} \text{ stage}}{\frac{JE + 1}{2}} \times \frac{KE + 1}{2} \Rightarrow IE \times JE \times KE$$

It is clear that the numbers  $(IE + 3)/4$ ,  $(JE + 3)/4$  and  $(KE + 3)/4$  must be integers. The transfer of the primitive variables from the coarse grid to the fine one is obtained by the following equations (Figure 3):

$$U_1 = (9U_{A'} + 3U_{B'} + 3U_{D'} + U_{C'})/16, \quad U_2 = (9U_{B'} + 3U_{A'} + 3U_{C'} + U_{D'})/16$$

$$U_3 = (9U_{C'} + 3U_{B'} + 3U_{D'} + U_{A'})/16, \quad U_4 = (9U_{D'} + 3U_{A'} + 3U_{C'} + U_{B'})/16$$

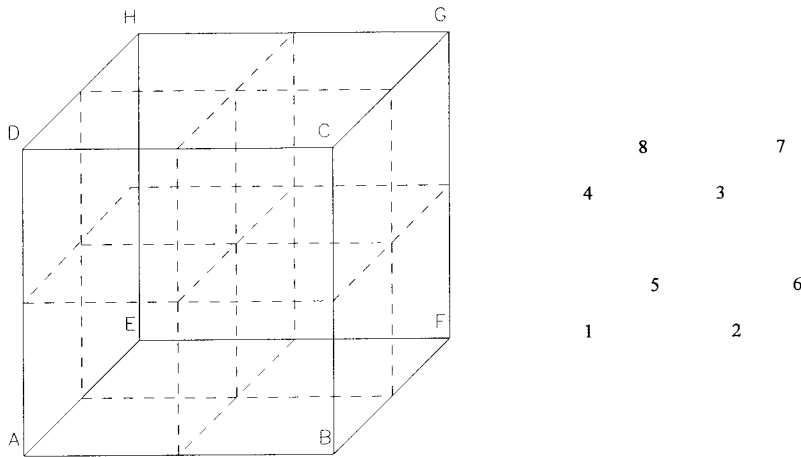


Figure 3. Presentation of the mesh-sequencing scheme.

$$U_5 = (9U_E + 3U_F + 3U_H + U_G)/16, \quad U_6 = (9U_F + 3U_E + 3U_G + U_H)/16$$

$$U_7 = (9U_G + 3U_F + 3U_H + U_E)/16, \quad U_8 = (9U_H + 3U_E + 3U_G + U_F)/16$$

where

$$U_{A'} = (3U_A + U_E)/4, \quad U_{B'} = (3U_B + U_F)/4, \quad U_{C'} = (3U_C + U_G)/4, \quad U_{D'} = (3U_D + U_H)/4$$

$$U_E = (3U_E + U_A)/4, \quad U_F = (3U_F + U_B)/4, \quad U_G = (3U_G + U_C)/4, \quad U_H = (3U_H + U_D)/4$$

A reduction of 50% of the computing time was reached in comparison with the computing time without the application of the mesh-sequencing scheme.

### 3. NUMERICAL RESULTS AND VALIDATION

#### 3.1. Laminar and turbulent flow through a square duct a with 90° bend (three-dimensional flow)

The present numerical method is applied to the case of the steady flow through a square duct with a 90° bend. The case was studied experimentally by Taylor *et al.* [30] and the detailed geometry of the bend is given in Figure 4. Two different grids,  $81 \times 13 \times 21$  and  $101 \times 21 \times 41$  (in the streamwise, normal and radial directions respectively) were used and formed in one half of the symmetric duct (the flow is symmetric) between the symmetry plane [AFGD]  $z/z_{1/2} = 0$  and the plane of the right side [BEHC] of the duct  $z/z_{1/2} = 1.0$ . The grid  $81 \times 17 \times 33$  is shown in Figure 5. For the acceleration of the convergence, the grid nodes are finer near the solid walls. Two cases are examined. A laminar flow with  $Re = 790$  and a turbulent flow with  $Re = 40000$ . The Reynolds number ( $Re = U_{in} \cdot L_{in} / \nu$ ) is defined using the average inlet velocity ( $U_{in}$ ) as the unit velocity and the side of the square cross-section as the unit length ( $L_{in}$ ). The boundary conditions are given in Table I. The inlet section is located 7.5 length units upstream of the bend and the outlet section is 15 units downstream of the bend.

For the laminar flow case  $Re = 790$ , the obtained numerical velocity results are compared with the experimental measurements of Taylor *et al.* [30] (Figure 6). The streamwise-velocity profiles are given at two sections upstream of the curved section,  $x = -0.5$  and  $x = -0.25$ , at three positions in the curved section corresponding to  $\theta = 30^\circ$ ,  $60^\circ$  and  $77.5^\circ$  and at three sections upstream of the bend, namely at  $x = 0.25$ ,  $x = 0.4$  and at  $x = 2.5$ . At each section along the duct, the velocity values are plotted for five radial locations between the inner ( $r = r_i$ ) and the outer ( $r = r_o$ ) curved wall. On the same Figure 6, velocity profiles corresponding to two different grids:  $81 \times 13 \times 21$  and  $101 \times 21 \times 41$  nodes are also given in order to examine the grid-independence of the solution.

The obtained results are compared in Figure 7, with the corresponding results obtained by a finite difference based numerical method from Sotiropoulos *et al.* [31]. The application of the

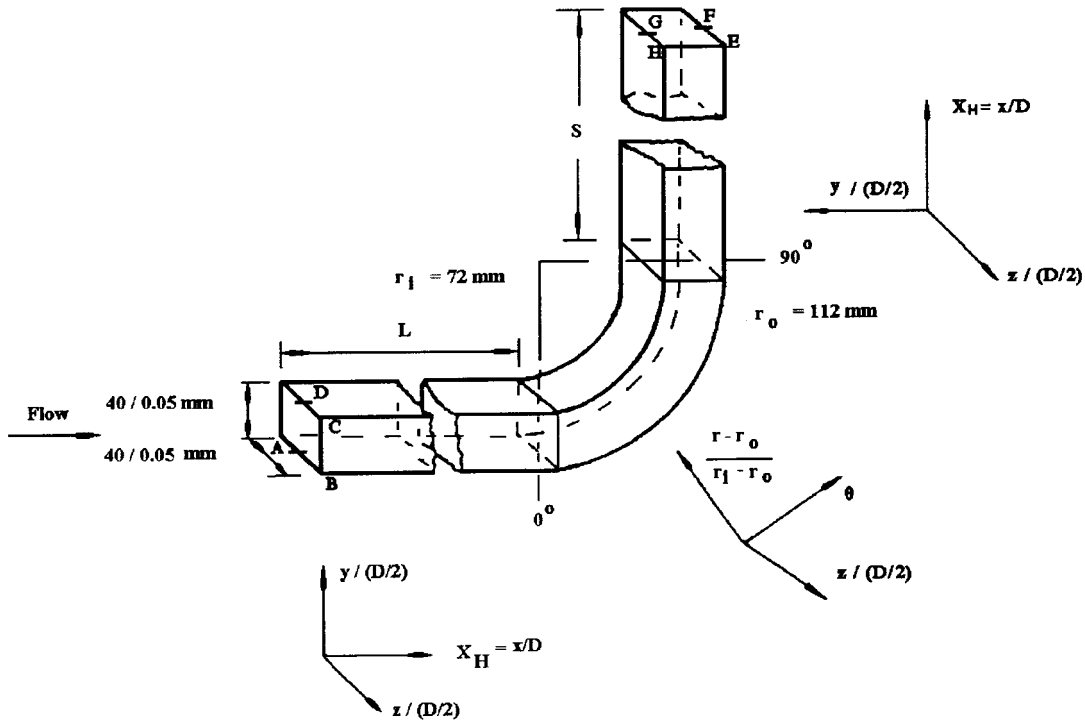


Figure 4. Geometry of the square duct with  $90^\circ$  bend.

last method is carried out on a numerical grid with  $69 \times 21 \times 41$  nodes. The measured and current calculated velocity profiles along  $z$ -lines at the sections  $x = -0.25$ , downstream of the bend, at  $\theta = 30^\circ, 77.5^\circ$  in the curved duct, and at  $x = 0.25$  and  $x = 2.5$  upstream of the bend are given in Figure 8.

At the other sections of the duct the current calculations are in good agreement with the experimental data and with the other numerical results. In the Figures 6–8, it is clear that the obtained results are independent from the density of the computational grid.

In the second case of the turbulent flow, where the Reynolds number is equal to  $Re = 40000$ , the numerical solution is carried out on the grid with  $81 \times 13 \times 21$  nodes. In Figure 9, the current numerical streamwise-velocity profiles are compared with the experimental measurements of Taylor *et al.* [30]. The velocity profiles are given at a section upstream of the bend,  $x = -0.25$ , at three sections in the curved part of the duct corresponding to  $\theta = 30^\circ, 60^\circ$  and  $77.5^\circ$  and at two sections upstream of the bend, at  $x = 0.25, x = 0.4$  and  $x = 2.5$ . The comparison is good, although some discrepancies exist near the upper solid wall ( $r = r_i$ ) on the curved section of the duct. The main reason for this is that the grid density is not fine enough to predict exactly the sharp variation of the flow in this section of the duct.

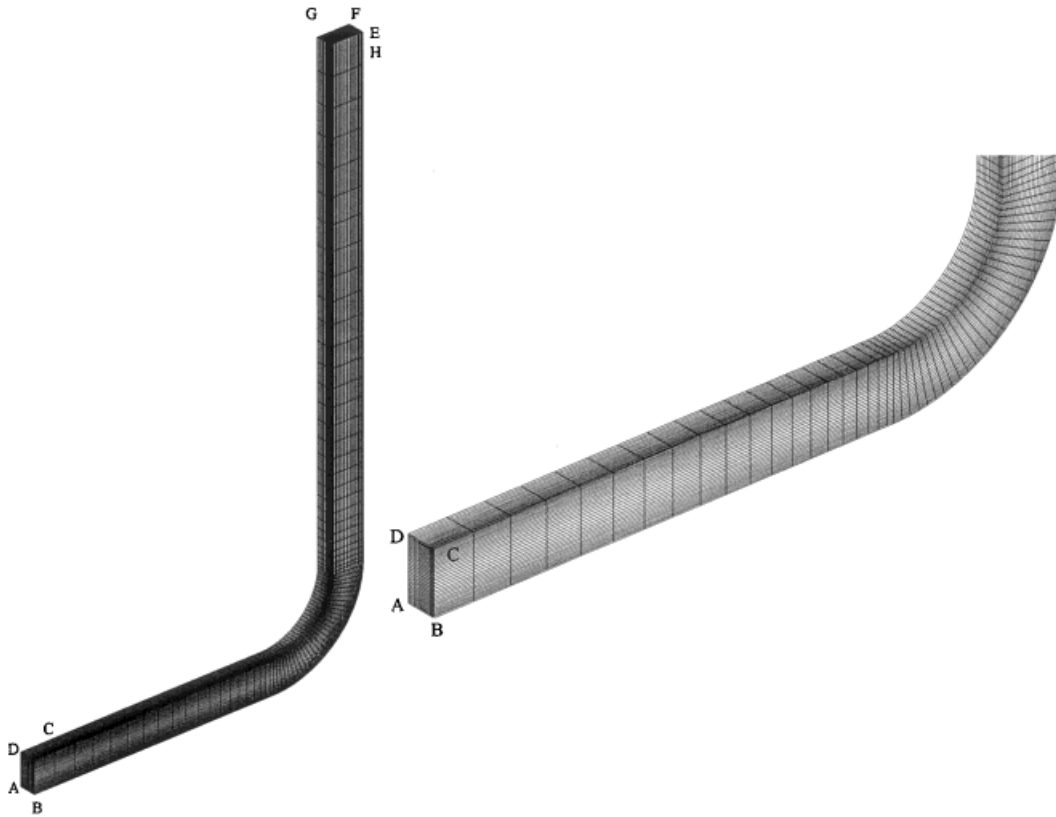


Figure 5. Numerical grid  $81 \times 13 \times 21$  of square duct with  $90^\circ$  bend.

Table I. Boundary conditions.

Plane	
[CDGH]	Solid wall conditions
[BCHE]	Solid wall conditions
[ABEF]	Solid wall conditions
[ADGF]	Symmetry wall conditions
[ABCD]	Inlet boundary conditions with uniform velocity profile
[EFGH]	Outlet boundary conditions with constant reference static pressure

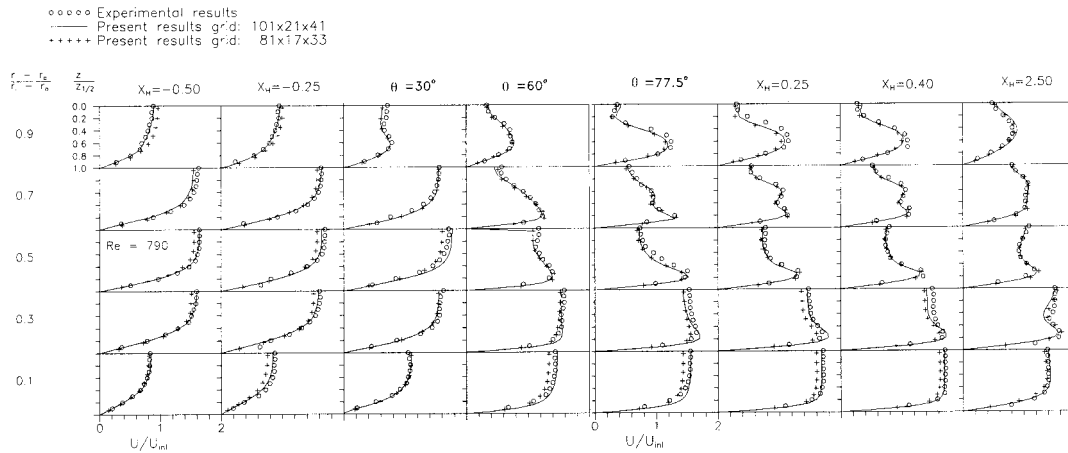


Figure 6. Comparison between present and experimental streamwise-velocity profiles for  $Re = 790$ .

Finally, in Figures 10 and 11 the convergence histories for both cases ( $Re = 790$  and  $40000$ ) for single grid calculation and for mesh-sequencing technique are shown. By the application of the mesh-sequencing scheme, the run-time is reduced by about 50% in comparison with the single grid calculation.

### 3.2. Flow through the SHF pump impeller

The SHF impeller is a radial centrifugal impeller with seven blades. The impeller was designed within the Working Group of the Societe Hydrotechnique de France (SHF) in order to study the inlet and outlet recirculations in centrifugal pumps at partial flow rates. Similar impellers have been tested in air and in water in different American and European laboratories and institutes with various test conditions. Many universities and companies have tested their three-dimensional numerical codes (Euler, boundary layer, Navier–Stokes codes) using the three-dimensional flow case of the SHF impeller, and comparisons have been made with the experimental results for different flow rates.

The impeller geometry and the main characteristics are given in Figure 12. The nominal flow rate of water in the impeller is  $0.1118 \text{ m}^3 \text{ s}^{-1}$  and it corresponds to a mean axial velocity of  $3.04 \text{ m s}^{-1}$ . The nominal head is 31 mWG and the rotational speed is 1200 rpm, which corresponds to a peripheral velocity of  $25.13 \text{ m s}^{-1}$ . The Reynolds number ( $Re = V \cdot D / \nu$ ) is equal to  $Re = 650000$ , where  $V$  is the mean inlet axial velocity ( $3.04 \text{ m s}^{-1}$ ) and  $D$  is the inlet diameter of the impeller (220 mm).

For simplicity, the impeller is regarded as a free rotor, in which the flow behaviour is independent of the diffuser and the volute. Especially for flow rates different than the nominal

- Experimental (Taylor *et al.* [30]) results
- Present results grid: 101x21x41
- △△△△△ Sotiropoulos *et al.* [31] grid: 69x21x41

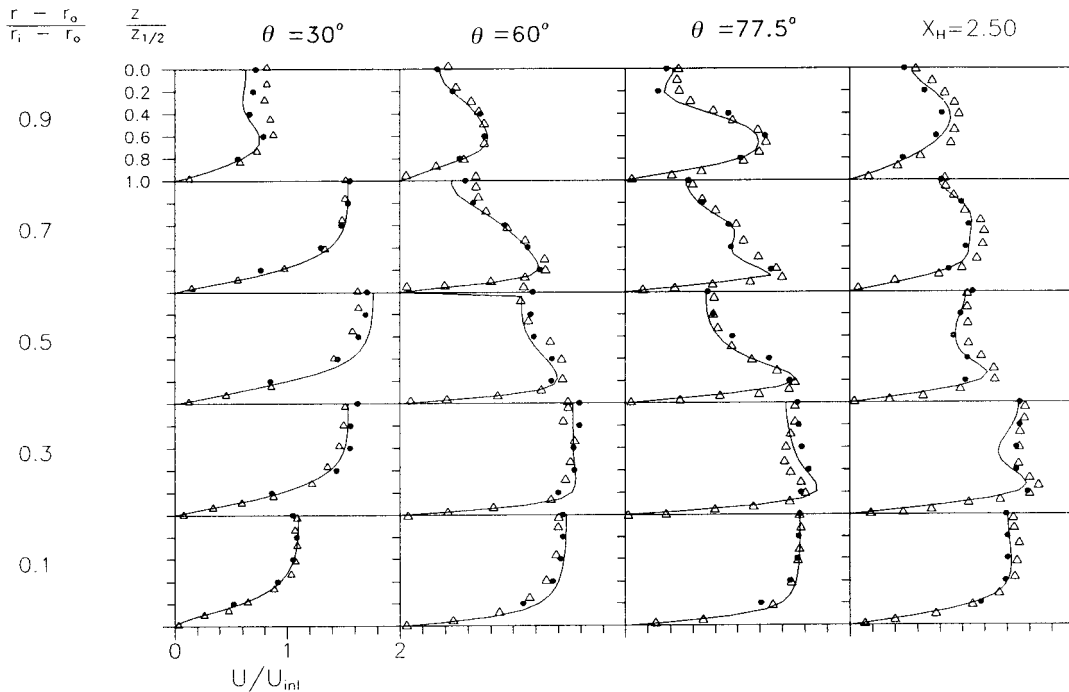


Figure 7. Comparison between numerical and experimental streamwise-velocity profiles for  $Re = 790$ .

one, this assumption is not accurate as flow interaction effects appear between the impeller and the spiral casing.

In the present analysis, computations are carried out for two flow rates: nominal ( $Q = Q_n$ ) and partial flow rate ( $Q = 60\% Q_n$ ).

In this paper, two sets of experimental measurements are referred: (a) LDV discharge data [32] performed at Institut National des Sciences Appliquées (INSA) in Lyon on a water model for five flow rates, and (b) static pressure measurements [33] performed at École Nationale Supérieure d'Arts et Métiers (ENSAM) in Lille on an air model for different flow rates. Apart from the experimental measurements, the current results are also compared with numerical results obtained by another finite volume Navier–Stokes code, which was developed by Sulzer Company [34].

Assuming periodic flow conditions through the impeller, the computational domain is restricted to one impeller channel. The blades are part of the boundary. The channel is extended upstream with part of the inlet pipe and downstream by an unvaned diffuser. Inflow

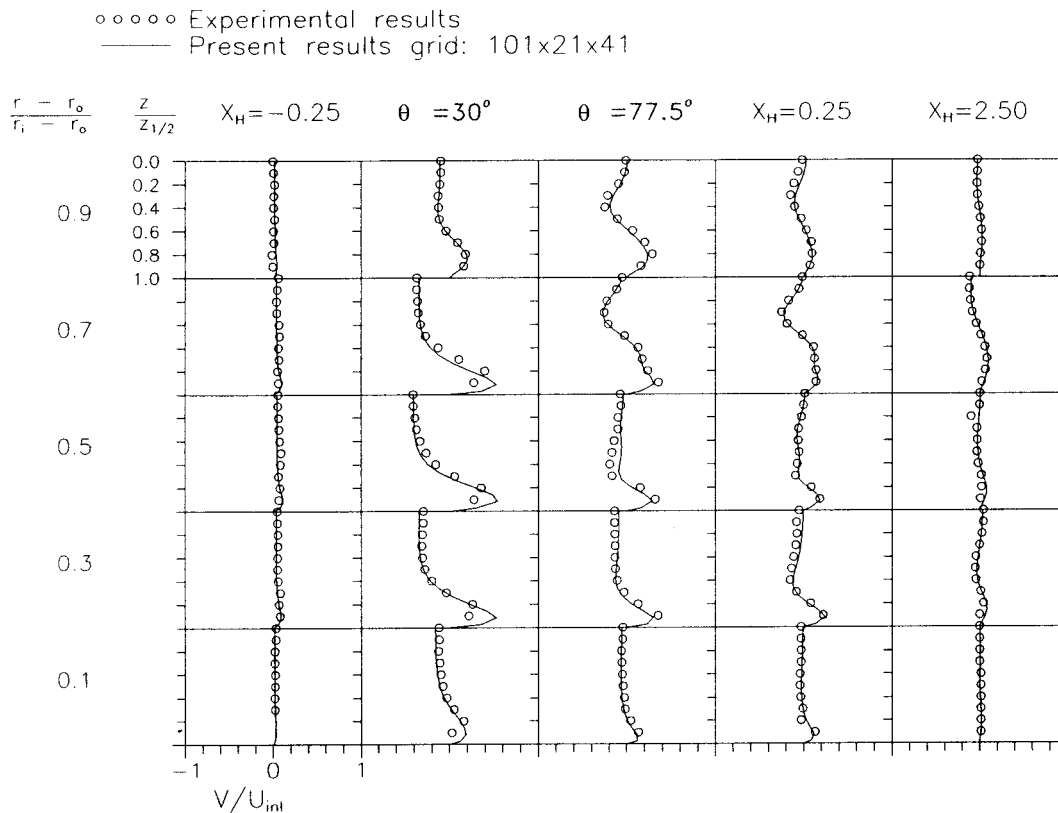


Figure 8. Measured and calculated radial velocity profiles along  $z$ -lines for  $Re = 790$ .

axial velocity at the inlet corresponds to the appropriate flow rate. As the considered domain is rotating with angular velocity  $\omega$ , the inflow relative peripheral velocity is equal to  $-\omega r$ . At the outflow, the pressure is taken equal to its reference value and the second derivative of the relative velocity is set equal to zero. On the blades, the hub and the shroud, the velocity components are equal zero and the standard wall functions are applied.

The reference grid (Figure 13) has 27 nodes from hub to shroud ( $K$ -direction) and 27 nodes from the suction side of one blade to the pressure side of the next blade ( $J$ -direction). From the inlet to the outlet ( $I$ -direction), 79 nodes are located. The leading edge corresponds to  $I=13$  and the trailing edge to  $i=67$ . The grid consists of 57571 nodes, which are not uniformly distributed as their density is more important near the solid walls. The outlet diameter of the impeller is 400 mm and the outlet diameter of the computational domain is taken equal to 475 mm.

Computations have been performed on a Silicon Graphics Power Challenge XL (MIPS 270 spsfp 92) using one processor. For a single grid calculation (without using the

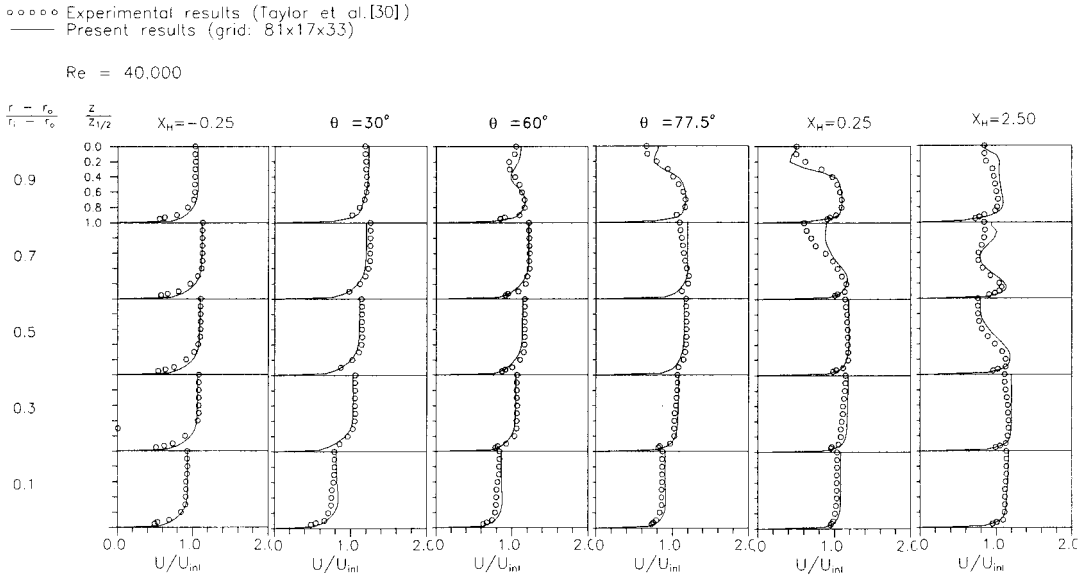


Figure 9. Comparison between present and experimental streamwise-velocity profiles for  $Re = 40000$ .

mesh-sequencing scheme), CPU time was 383 min for  $Q/Q_n = 100\%$  flow case and 526 min for  $Q/Q_n = 60\%$  flow case.

The existing static pressure measurements are distributed along both sides of the blade, the hub and the shroud in the impeller region. Current computations of the static pressure at the hub and at the shroud, along the centreline, are given in Figures 14 and 15 for the case of the nominal flow rate ( $Q = Q_n$ ) and for the case of the part flow rate ( $Q/Q_n = 60\%$ ) respectively. In Figure 16, the distribution of the pressure, along both sides, is given for the two flow cases. In all figures, the current results are well correlated to the experimental measurements and the Sulzer Company data. The comparison shows that computed pressures correspond quite well to measurements, except near the trailing edge and near the leading edge at the shroud side, due to losses.

Pitch-averaged relative velocities are plotted in Figures 17 and 18 for the nominal flow rate, where the trailing edge radius is given by  $r_2 = 200$  mm. Radial and tangential relative velocity components are given as a function of the axial position, from the hub to the shroud, for two radial positions: in the impeller ( $r/r_2 = 0.818$ ) and in the diffuser ( $r/r_2 = 1.018$ ). The velocities of the calculations are also mass-averaged according to the following formulas:

$$\bar{c}_{rad} = \frac{\iint c_{rad}^2 dA}{\iint c_{rad} dA} \quad [m s^{-1}]; \quad \bar{c}_{tang} = \frac{\iint c_{rad} c_{tang} dA}{\iint c_{rad} dA} \quad [m s^{-1}],$$

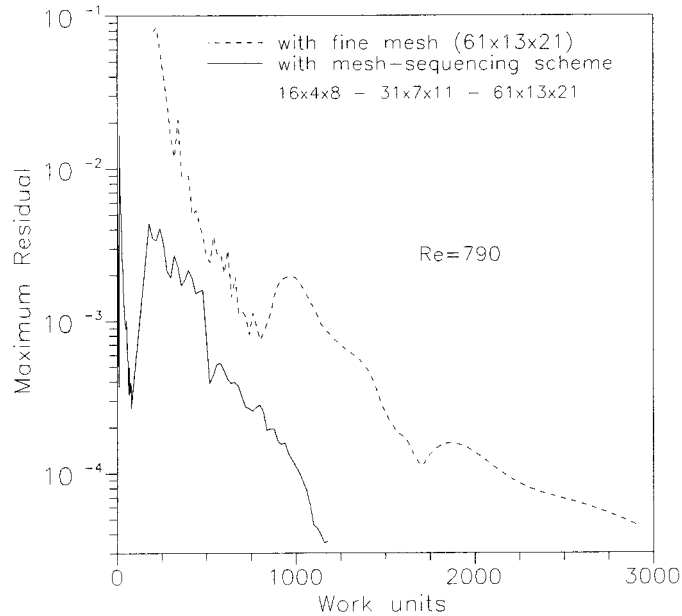


Figure 10. Convergence history for the single-grid ( $81 \times 13 \times 21$ ) calculation and mesh-sequencing ( $21 \times 4 \times 6 \rightarrow 41 \times 7 \times 11 \rightarrow 81 \times 13 \times 21$ ) calculation, for  $Re = 400$ .

It shows calculations obtained by the current method and the Sulzer Company method, as well as flow measurements performed at INSA. In both radial positions, the average radial velocity as computed by the present method agrees quite well with measurements, although the slightly higher radial velocity component near the shroud is not predicted by the numerical results. Computed pitch-averaged tangential velocity components show a reasonable agreement with experiments.

Figures 19 and 20 show radial and tangential relative velocity profiles near the impeller exit ( $r/r_2 = 0.978$ ), for the nominal flow rate ( $Q/Q_n = 100\%$ ) and for the part flow rate ( $Q/Q_n = 60\%$ ) respectively, and for the located points at the mid-channel ( $b/b_{\max} = 0.5$  to  $0.52$ ). The radial velocity component predicted by the current method agrees well with experimental data, both for nominal and partial flow rates. However, at the nominal flow rate, large deviations still occur near the suction side (SS) of the blade. The numerical tangential velocity profiles show good agreement with experimental measurements both for nominal and partial flow rate.

Finally Figure 21 shows the hub–shroud distribution of the streamwise relative velocity at mid-pitch for the nominal and the partial flow rates. For the case of the partial flow rate, the generation of a small recirculation zone is observed upstream of the leading edge and near the shroud side.

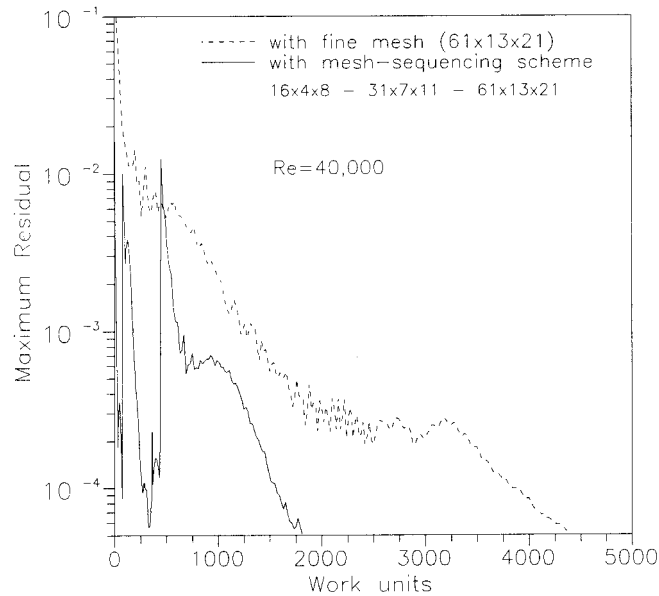


Figure 11. Convergence history for the single-grid ( $81 \times 13 \times 21$ ) calculation and mesh-sequencing ( $21 \times 4 \times 6 \rightarrow 41 \times 7 \times 11 \rightarrow 81 \times 13 \times 21$ ) calculation, for  $Re = 40000$ .

#### 4. CONCLUSIONS

The objective of the present work was to develop a numerical method for the solution of the three-dimensional steady turbulent flows in hydraulic turbomachines and installations. The study solved the fluid flow equations via a new characteristic based method. The continuity and momentum equations were coupled by the introduction of the artificial compressibility formulation and a hyperbolic set of equations for the inviscid incompressible case was derived. The standard  $k-\varepsilon$  equations were used for modelling the turbulence and wall effects in turbulent flows were taken into account by the use of the law of the wall. For the time integration, an explicit Runge–Kutta scheme was used.

The validation of the algorithm is performed on the numerical prediction of the three-dimensional flow (laminar and turbulent) through a square duct with a  $90^\circ$  bend and the flow through the SHF radial water pump impeller. The computations show a qualitative agreement with experimental measurements, and the method provides an enough high accuracy.

Several improvements to the current code could be carried out in the near future as the application of a local multigrid scheme or the application of an implicit formulation of the characteristic based method in order to accelerate the convergence. Finally, the method could be extended to the unsteady three-dimensional flows.

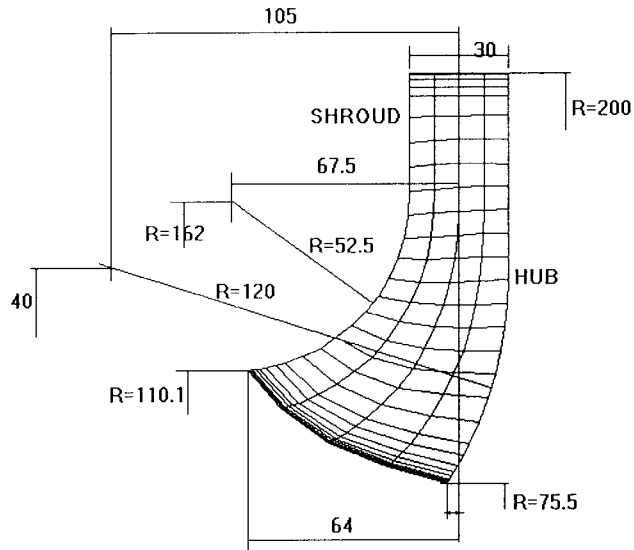


Figure 12. Geometry and main characteristics of the SHF pump impeller.

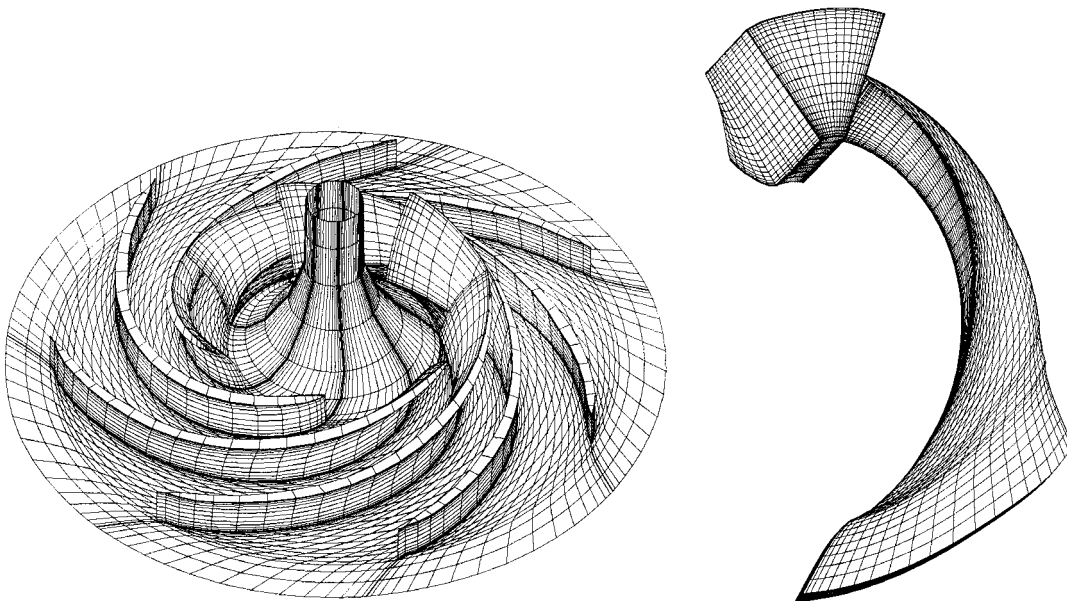


Figure 13. Numerical grid  $79 \times 27 \times 27$  of the SHF impeller blade.

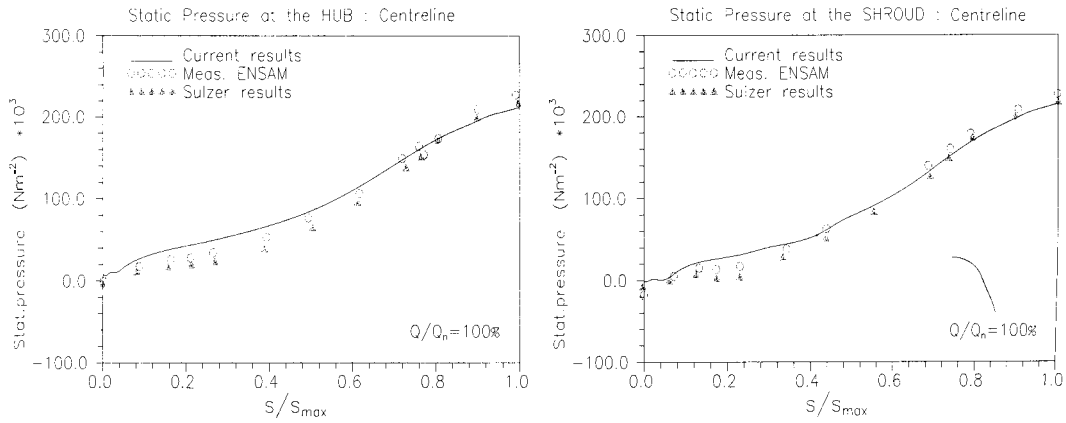


Figure 14. Correlation of measured and computed values of static pressure at centreline of hub and shroud, for nominal flow rate ( $Q/Q_n = 100\%$ ).

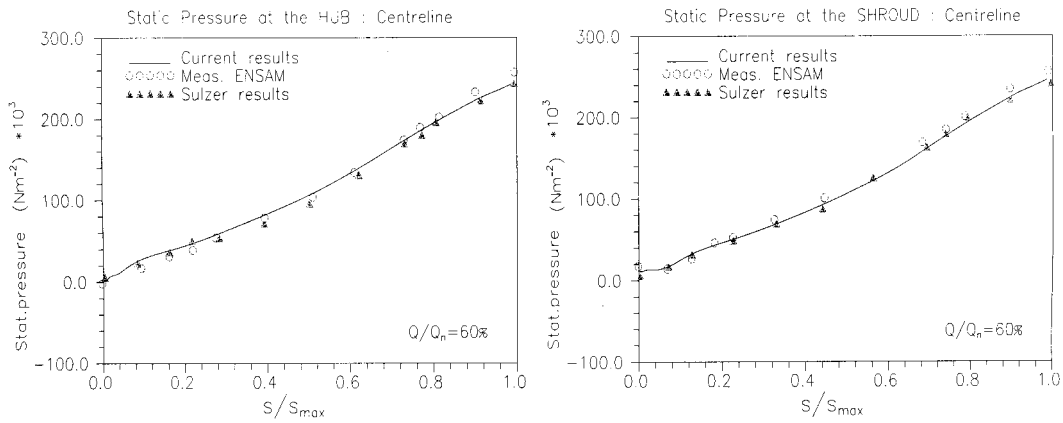


Figure 15. Correlation of measured and computed values of static pressure at centreline of hub and shroud for partial flow rate ( $Q/Q_n = 60\%$ ).

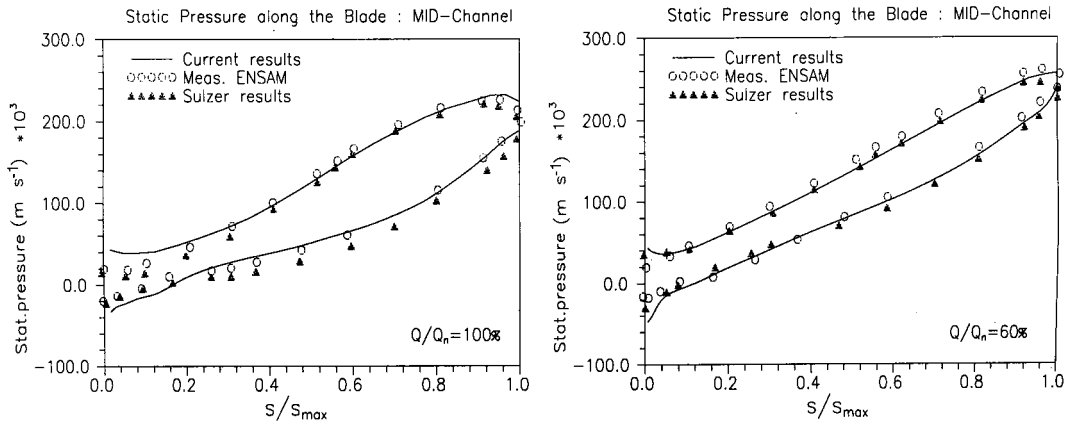


Figure 16. Correlation of measured and computed values of static pressure along the blade for nominal ( $Q/Q_n = 100\%$ ) and partial flow rate ( $Q/Q_n = 60\%$ ).

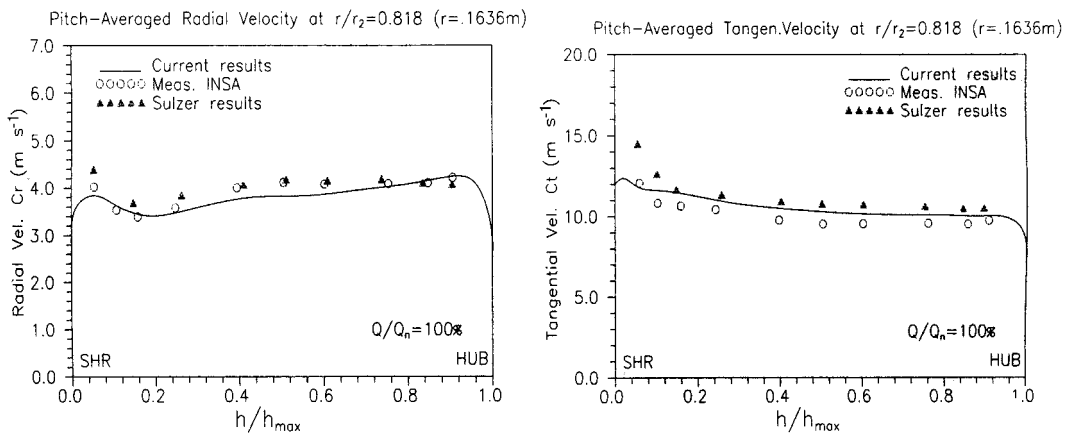


Figure 17. Averaged velocity components at  $r/r_2 = 0.818$ , for nominal flow rate ( $Q/Q_n = 100\%$ ).

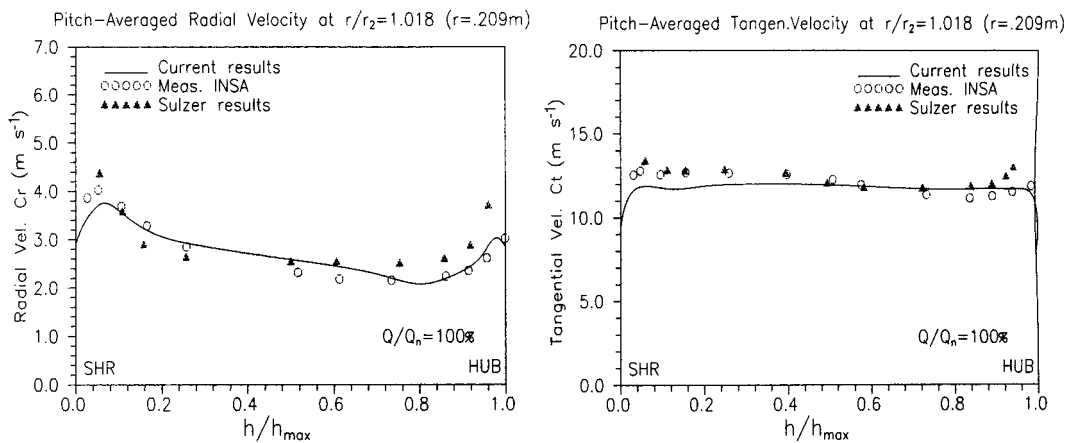


Figure 18. Averaged velocity components at  $r/r_2 = 1.018$ , for nominal flow rate ( $Q/Q_n = 100\%$ ).

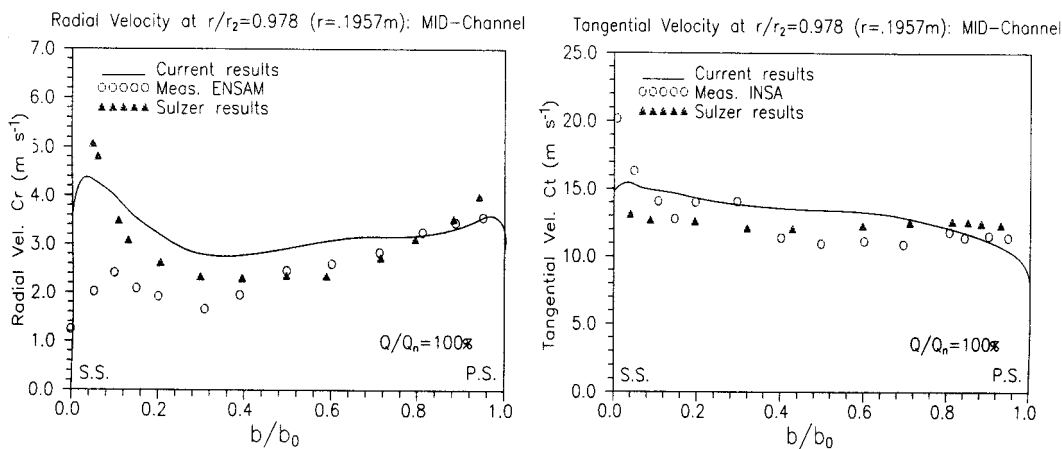


Figure 19. Velocity profiles at  $r/r_2 = 0.978$ , for nominal flow rate ( $Q/Q_n = 100\%$ ). The left side is the suction side of the blade, the right side is the pressure side.

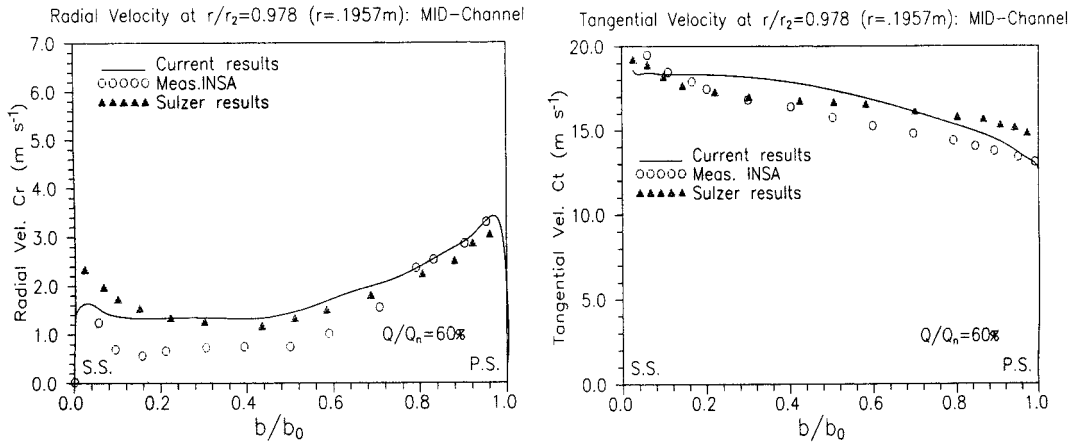


Figure 20. Velocity profiles at  $r/r_2 = 0.978$ , for partial flow rate ( $Q/Q_n = 60\%$ ). Orientation of suction side and pressure side as in Figure 19.

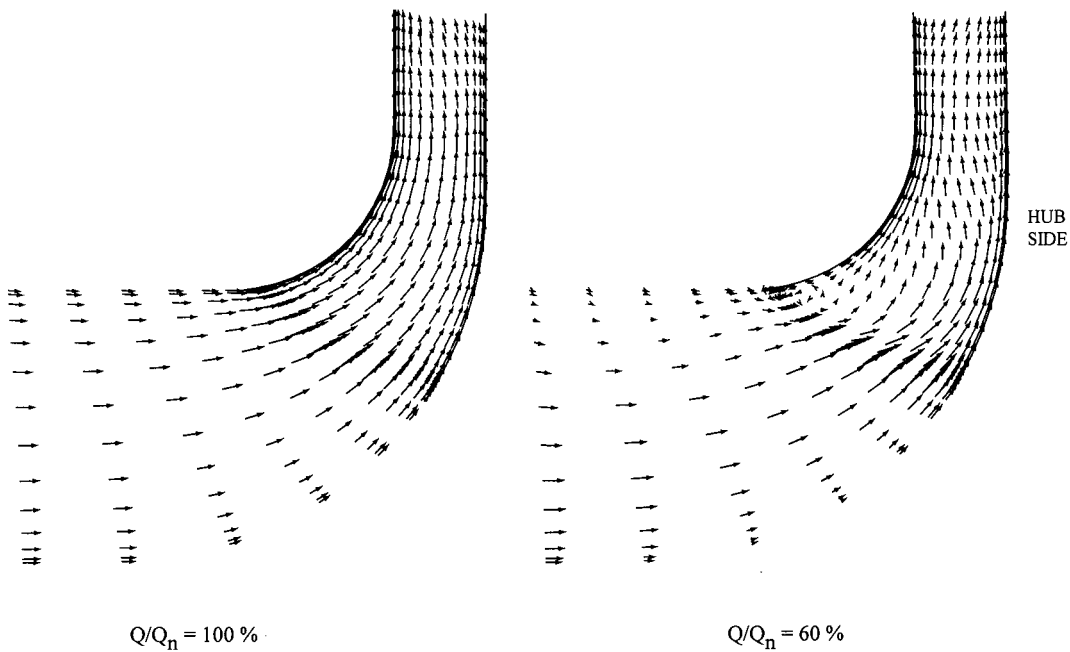


Figure 21. Hub-shroud distribution of the streamwise-velocity at mid-pitch for nominal and partial flow rate.

## REFERENCES

1. Bosman C, Ahrabian D. Calculation of stalled flow in a centrifugal impeller. *IMechE* 1984; **C**: 67–84.
2. Nakao S-I. Turbulent flow in square ducts after an expansion. *AIAA Journal* 1986; **24**(6): 979–982.
3. Wilkinson DH. A numerical solution of the analysis and design problems for the flow past one or more aerofoils or cascades. ARC Reports and Memoranda No. 3545, 1967.
4. Ribaut M. 3D calculation of flow in turbomachines with the aid of singularities. *Transactions of the ASME, Journal of Engineering and Power* 1968; **90**(3): 674–683.
5. Horlock JH, Marsh H. Flow models for turbomachines. *Journal of Mechanical Engineering Science* 1971; **13**(5): 00–00.
6. Fisher RK, Colwill WH, Chacour SA. Computer aided pump and turbine design. The results after six years. IAHR-Symposium, Montreal, 1986.
7. Keck H, Goede E, Grunder R, Pestalozzi J. Upgrading by new runners based on 3D-Euler simulation and model testing. IAHR-Symposium, Sao Paulo, 1992.
8. Goede E, Cuenod R. Numerical flow simulations in Francis turbines. *Water Power and Dam Construction* 1989; **May**: 23–27.
9. Thibaud F, Drotz A, Sottas G. Validation of an Euler code for hydraulic turbines. AGARD Symposium Lisbon Portugal, May, 1988.
10. Badie R, Jonker JB, van Essen TG. Calculations on the time-dependent potential flow in a centrifugal pump. ASME Paper No. 92-GT-151, 1992.
11. Govatsos P, Papantonis D. A Navier–Stokes solver for incompressible flows based on the method of characteristics. In *Proceedings of the 4th Greek National Congress on Mechanics*, vol. II, 1995; 906–915.
12. Govatsos P, Papantonis D. Three dimensional study of the flow in hydraulic turbine draft tubes based on a characteristic method for incompressible flows. GAMM Symposium, Prague, 1996.
13. Harlow FH, Weelch JE. Numerical calculation of time dependent viscous incompressible flow with free surface. *Physics of Fluids* 1965; **8**: 2182–2189.
14. Armaly BF, Durst F, Pereira JCF, Schonung B. Experimental and theoretical investigation of backward-facing step flow. *Journal of Fluid Mechanics* 1983; **127**: 473–496.
15. Chorin AJ. A numerical method for solving incompressible viscous flow problems. *Journal of Computational Physics* 1967; **2**: 12–26.
16. Kwack D, Chang JL, Shanks SP, Chakravarthy SR. A three dimensional Incompressible flow solver using primitive variables. *AIAA Journal* 1986; **24**(3): 390–396.
17. Merkle C, Athavale AA. Time accurate unsteady incompressible flow algorithms based on artificial compressibility. AIAA Paper No. 87-1137, 1987.
18. Drikakis D, Govatsos PA, Papantonis D. A characteristic-based method for incompressible flows. *International Journal for Numerical Methods in Fluids* 1994; **19**: 667–685.
19. Ramshaw JD, Mesina GL. A hybrid penalty-pseudocompressibility method for transient incompressible fluid flow. *Computer and Fluids* 1991; **20**(2): 165–175.
20. Eberle A. 3D Euler calculations using characteristic flux extrapolation. AIAA Paper No. 85-0119, 1985.
21. Drikakis D, Tsangaris S. On the solution of the compressible Navier–Stokes equations using improved flux vector splitting methods. *Applied Mathematics Modelling* 1993; **17**: 282–297.
22. Drikakis D, Tsangaris S. An implicit characteristic flux averaging scheme for the Euler equations for real gases. *International Journal for Numerical Methods in Fluids* 1991; **12**: 771–776.
23. Launder BE, Spalding DE. The numerical computation of turbulent flows. *Computer Methods in Applied Mechanics and Engineering* 1974; **3**: 269–289.
24. Hirsch C. *Numerical Computation of Internal and External Flows*, vol. I. Wiley: New York, 1988.
25. Kunz RF, Lakshminarayana B. Explicit Navier–Stokes computation of cascade flows using the  $k-\epsilon$  turbulence model. *AIAA Journal* 1992; **30**(1): 13–22.
26. Eberle A. Characteristic flux averaging approach to the solution of Euler's equations. VKI Lecture Series, 1987-04, 1987.
27. Shi Q, Ribando RJ. Numerical simulations of viscous rotating flows using a new pressure-based method. *Computers and Fluids* 1992; **21**(4): 475–489.
28. Elkaim D, Reggio M, Camarero R. Simulating two-dimensional turbulent flow by using  $k-\epsilon$  model and the vorticity–streamfunction formulation. *International Journal of Numerical Methods in Fluids* 1992; **14**: 961–980.
29. Drikakis D. Development of upwind numerical methods in high speed aerodynamics. PhD thesis, National Technical University of Athens, Greece, 1991.
30. Taylor AM, Whitelaw JH, Yianneskis M. Measurements of laminar and turbulent flow in a curved duct with thin inlet boundary layer. NASA Contractor Report 3367, 1981.

31. Sotiropoulos F, Kim W, Patel V. A computational comparison of two incompressible Navier–Stokes solvers in three-dimensional laminar flows. *Computers and Fluids* 1994; **23**(4): 627–646.
32. Combes JF, Rieutord E. Numerical and experimental analysis of the flow in a centrifugal pump at nominal and partial flow rate. ASME Paper No. 92-GT-284, 1992.
33. Morel P. Ecoulements décolles dans une roue de pompe centrifuge. Conception et réalisation d’un banc d’essai. Analyse des pressions parietales. PhD thesis, Université de Lille, France, 1993.
34. Muggli F. Test case 5: SHF radial pump TASCflow simulation. ERCOFTAC Seminar and Workshop on 3D Turbomachinery Flow Prediction, January, 1995.